Check for updates

Molecular modeling studies of 1,2,4-triazine derivatives as novel h-DAAO inhibitors by 3D-QSAR, docking and dynamics simulations†

Ping Ping Qian, Shuai Wang, Kai Rui Feng and Yu Jie Ren ![ORCID] *

Human D-amino acid oxidase (h-DAAO) can effectively act on D-serine, which has been actively explored as a novel therapeutic target for treating schizophrenia. In this study, 37 h-DAAO inhibitors based on a 6-hydroxy-1,2,4-triazine-3,5(2H,4H)-dione scaffold were obtained to construct the optimal comparative molecular field analysis (CoMFA, $q^2 = 0.613$, $r^2 = 0.966$) and comparative molecular similarity index analysis (CoMSIA, $q^2 = 0.669$, $r^2 = 0.985$) models. The results indicate that the models have good predictability and strong stability. Furthermore, contour maps of the three-dimensional quantitative structure–activity relationship (3D-QSAR) revealed the relationships between the structural features and inhibitory activity. A total of nine new h-DAAO inhibitors were designed, which exhibited good predicted pIC_{50} values. Through molecular docking and molecular dynamics simulation, four essential residues (*i.e.*, Gly313, Arg283, Tyr224 and Tyr228) were considered to interact with the inhibitor. The hydrogen bonds produced by the triazine structure with protein and the hydrophobic interactions with the residues (*i.e.*, Leu51, His217, Gln53 and Leu215) play an important role in the stability of the inhibitor at the binding site of the protein. Additionally, the compounds **D1**, **D3** and **D8**, with higher predicted activities, were selected by ADME and bioavailability prediction. The present study could offer a reliable theoretical basis for future structural optimisation, design and synthesis of effective antipsychotics.

Introduction

Schizophrenia can be literally interpreted as a 'shattered mind'. It is among the top 10 causes of long-term disability that affects approximately 24 million people worldwide.[1] Symptoms of schizophrenia mainly include hallucinations, delusions, and disordered thoughts and emotions. Schizophrenia also poses the risk of suicide or even murder. Additionally, young people are prone to suffering from schizophrenia, and it causes an enormous burden to society.[2] In recent years, developing countries have increasingly reported that the deaths of schizophrenics, including undergraduates, postgraduates, PhD students, white-collar workers, laid-off workers, *etc.*, result from education and employment pressures. Furthermore, most patients with schizophrenia are not appropriately treated. The current methods for treating schizophrenia include electroconvulsive therapy and positive psychotherapy,[3,4] but drug treatment remains the most effective and widely accepted.[5] Therefore, there is an urgent need for effective and safe antipsychotic drugs.

Over the past few decades, all typical and second-generation antipsychotics that act on the D2 dopamine receptor (*e.g.*, perphenazine,[6] clozapine,[7] olanzapine,[8] risperidone,[9] ziprasidone[10] and aripiprazole[11]) have caused considerable metabolic and negative side effects.[12] In addition, only a small number of patients have completely responded to these currently available antipsychotics, which cannot satisfy the requirements of patients with different etiologies. The situations necessitate new antipsychotics that will facilitate the antipsychotic target from the D2 dopamine receptor to the *N*-methyl-D-aspartate (NMDA) receptor. D-Serine, which is a full agonist at the glycine modulatory site of the NMDA receptor, has recently been actively explored as a therapeutic target for the treatment of schizophrenia.[13] Human D-amino acid oxidase (h-DAAO) is a peroxidase that catalyzes the oxidation of D-serine to H_2O_2 and the corresponding α-keto acids.[14] There is compelling evidence that the inhibition of h-DAAO could provide dual beneficial effects of D-serine therapy, namely, the weakening of D-serine induced nephrotoxicity and the enhancement of D-serine bioavailability. Thus far, researchers have developed several representative h-DAAO inhibitors, including sodium benzoate (SB),[15] 5-chloro-benzo[*d*]isoxazol-3-ol (CBIO),[16,17] 5-methylpyrazole-3-carboxylic acid (AS057278)[18] and 4*H*-thieno [3,2-*b*]pyrrole-5-carboxylic acid (compound **0**)[19] (Fig. 1); however, some demerits still exist. For example, SB exerts relatively low antipsychotic efficiency and

School of Chemical and Environmental Engineering, Shanghai Institute of Technology, Shanghai 201418, China. E-mail: clab@sit.edu.cn
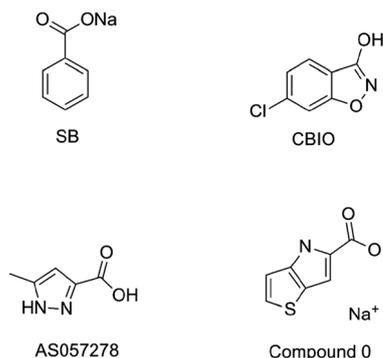
Fig. 1 Representative h-DAAO inhibitors.

requires high doses. In addition, although CBIO and AS057278 exhibit acceptable inhibitory potency against h-DAAO, their high acidity and low hydrophobicity hamper cell permeability. To overcome these drawbacks, researchers are continuously performing further studies on h-DAAO inhibitors, and many h-DAAO inhibitors with high activities have been reported in recent years.[20–25] Hin *et al.*[25] reported that some potent h-DAAO inhibitors (IC_{50} in the nanomolar range) based on the 1,2,4-triazine scaffold appear to be metabolically resistant to *O*-glucuronidation, which is contrary to other structurally-related h-DAAO inhibitors. Compared to other h-DAAO inhibitors, these potent h-DAAO inhibitors not only exhibit high efficiency but also have improved metabolic stability.

Computer-aided drug design (CADD) has greatly improved the success rate of drug design and provides new ideas for overcoming persistent ailments. It has been developed and widely used for anticancer drugs, anti-HCV drugs, anti-inflammatory drugs and anti-AIDS drugs,[26–29] but few studies on antipsychotic drugs have been conducted. Moreover, there has never been a study on h-DAAO inhibitors with a simultaneous combination of modeling, prediction, design, molecular docking and dynamics simulation. In the present work, 37 reported triazine compounds were used to obtain the optimal three-dimensional quantitative structure–activity relationship (3D-QSAR) model, and the contour maps of the 3D-QSAR revealed the relationships between structural features and inhibitory activity; a 'crab' conformation was initially proposed. The binding mode between the inhibitor and receptor protein was explored by molecular docking and molecular dynamics simulation. Finally, the newly designed compounds with higher predicted activities were selected by ADME and bioavailability prediction. This work was aimed at studying the effects of the substituents (type and position) of the benzene ring and the 1,2,4-triazine structure on the potency of h-DAAO inhibitors, which can be useful for further discovery, design and synthesis of new and effective anti-psychotics. Moreover, the interactions between h-DAAO and their inhibitors can be calculated, which can greatly shorten the development cycle. This study therefore provides a vital reference and guide for the emergence and development of novel, broad-spectrum and highly active h-DAAO inhibitors in the future.

Materials and methods

Computational approach

All calculations in this study were conducted using the SYBYL-X 2.0 software package (Tripos Inc., St. Louis, USA) in the Windows 7 OS. Three-dimensional structures of 1,2,4-triazine derivatives as h-DAAO inhibitors were built within the 2D sketch module and the initial conformations of molecules for 3D-QSAR were decided according to the conformation of the ligand extracted from the protein (PDB code: 3W4K). Energy optimization of all compounds was performed using Gasteiger–Hückel[30] charges under the impact of Tripos force field[31] parameters. During the optimization process, the Powell gradient algorithm with a maximum of 10 000 iterations was adopted, and the energy convergence criterion was limited to 0.005 kcal $(mol^{-1} Å^{-1})$. Both comparative molecular field analysis (CoMFA)[32] and the comparative molecular similarity index analysis (CoMSIA)[33] models were then developed by the QSAR module in SYBYL-X 2.0. In this calculation, all other parameters were set by default (except where noted).

Dataset

The total set of h-DAAO inhibitors used for the molecular modeling study was reported by Hin *et al.*[25] The structures and bioactivities of 1,2,4-triazine derivatives are described in Table 1 and the IC_{50} values were converted into pIC_{50} values (pIC_{50} = $-\log IC_{50}$), then they were used as the dependent variables. The range of pIC_{50} values was from 4 to 7.398, indicating that a broad date set with uniform density was used for the 3D-QSAR study. All the experimental data were divided into a training set of 31 compounds for model generation and a test set of the rest for model external validation without constraints. The accuracy of the selection criteria for the training and test set compounds was checked in the form of Uni-Column statistics,[34] as shown in Table 1S (see ESI data†). The maximum and minimum pIC_{50} values in the training and test sets meet the following requirements: (i) max (test) ≤ max (training) and (ii) min (test) ≥ min (training). The data set was output on the basis of substituent diversity and a well-proportioned distribution of biological data was taken (Fig. 1S†).
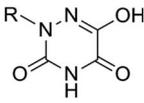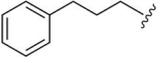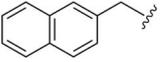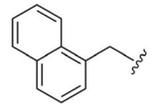
Alignment and generation of the 3D-QSAR models

Molecular alignment is regarded as the most important factor for 3D-QSAR analysis. In this study, the ligand-based alignment rule was adopted. The highest biological activity of compound **13** as the template molecule was employed and all the remaining compounds had to be well aligned with it for further analysis. Fig. 2a shows the structure of compound **13** and the red atoms represent the common structure. Fig. 2b illustrates the alignment results based on the common substructure of compound **13**.

For CoMFA analysis, steric and electrostatic fields were considered and computed on a spaced grid using a hybridized sp^3 carbon atom probe. In the case of CoMSIA analysis, five similarity index descriptors consisting of steric (S), electrostatic (E), hydrophobic (H), H-bond donor (D), and H-bond acceptor

Table 1 Molecular structures of all compounds involved in the study, their actual and predicted bioactivity for CoMFA and CoMSIA

Compound 1-9
Test 1-4

No.	R	Actual pIC$_{50}$	Predicted CoMFA	Residual	Predicted CoMSIA	Residual
1	CH$_3$	5.553	5.667	0.115	5.625	0.073
2		4.000	3.948	−0.052	4.026	0.026
3		5.770	5.574	−0.196	5.714	−0.056
4		6.658	6.712	0.055	6.631	−0.026
5		7.301	7.249	−0.052	7.332	0.031
6		7.000	6.887	−0.113	7.003	0.003
7		6.481	6.512	0.030	6.486	0.005
8		6.357	6.608	0.251	6.266	−0.091
9		6.509	6.874	0.366	6.469	−0.040
Test 1		6.585	6.177	−0.408	5.692	−0.893
Test 2		4.398	5.371	0.972	4.69	0.292
Test 3		5.292	5.284	−0.009	5.104	−0.188
Test 4		6.119	6.131	0.012	5.846	−0.273
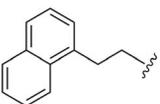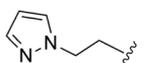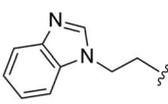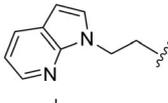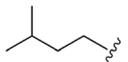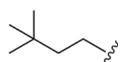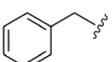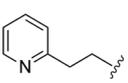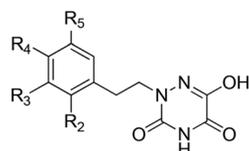
Compound 10-27
Test 5-6

No.	Substituents			Actual pIC$_{50}$	Predicted CoMFA	Residual	Predicted CoMSIA	Residual
	R$_2$	R$_3$	R$_4$					
10	H	H	H	7.155	7.144	−0.011	6.962	−0.193
11	Cl	H	H	7.000	6.997	−0.003	7.180	0.180

Table 1 (*Contd.*)

Compound 10-27
Test 5-6

	Substituents							
No.	R_2	R_3	R_4	Actual pIC_{50}	Predicted CoMFA	Residual	Predicted CoMSIA	Residual
12	H	Cl	H	7.222	7.062	−0.159	7.137	−0.085
13	H	H	Cl	7.398	7.118	−0.280	7.228	−0.170
14	F	H	H	7.097	7.137	0.040	7.081	−0.015
15	H	CH_3	H	7.155	6.955	−0.200	7.021	−0.134
16	H	H	CH_3	7.046	7.092	0.046	7.094	0.049
17	H	CF_3	H	7.000	6.883	−0.117	7.173	0.173
18	H	H	CF_3	7.097	7.088	−0.008	7.247	0.150
19	OCH_3	H	H	6.569	6.741	0.172	6.664	0.095
20	H	OCH_3	H	6.921	6.865	−0.056	6.909	−0.012
21	H	H	OCH_3	6.921	7.025	0.104	6.952	0.031
22	OH	H	H	7.046	7.027	−0.018	7.042	−0.004
23	H	OH	H	6.796	6.796	0.000	6.804	0.008
24	H	H	OH	6.959	6.918	−0.041	6.927	−0.032
25	H	OPh	H	6.620	6.751	0.131	6.684	0.064
26	H	H	OPh	7.097	7.087	−0.010	7.068	−0.029
27	H	H	Ph	7.301	7.307	0.006	7.315	0.014
Test 5	H	F	H	7.222	7.148	−0.074	7.003	−0.219
Test 6	H	H	F	7.301	7.151	−0.150	7.052	−0.249
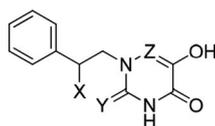
Compound 28-31

No.	X	Y	Z	Actual pIC_{50}	Predicted CoMFA	Residual	Predicted CoMSIA	Residual
28	CH_3	O	N	5.481	5.481	0.000	5.483	0.002
29	OH	O	N	6.328	6.383	0.055	6.324	−0.003
30	H	S	N	7.301	7.302	0.001	7.239	−0.062
31	H	O	CH	7.097	7.043	−0.054	7.146	0.049

(A) fields, were obtained in the same manner as described for CoMFA. Whether the five descriptors in CoMSIA are completely independent has been discussed in some papers.[35,36] Different combinations of these five fields were used to build the optimal CoMSIA model in this paper, and the cross-validated correlation coefficient (q^2) values of all combinations are shown in Fig. 2S.† The probable models with higher q^2 values ($q^2 > 0.6$) were selected (in green and red), including SE, SD, SEH, SED, SEA, SDA, SEHD, SEHA, SEDA and SEHDA (0.666, 0.663, 0.671, 0.668, 0.685, 0.667, 0.659, 0.646, 0.700 and 0.669, respectively). By comparison, the different combinations all have the steric field (S), illustrating that this is necessary for consideration in

CoMSIA analysis. According to the entire statistical parameter results of the ten combinations in Table 2, the five fields should all be considered for CoMSIA analysis. Finally, the best CoMSIA model was built based on the combination of SEHDA fields (in red).

Partial least squares (PLS) analysis and validation of the 3D-QSAR models

To attain more reliable 3D-QSAR models, partial least squares (PLS) regression analysis was carried out by using the leave-one-out (LOO) cross-validation, and the optimum number of components (ONC values) was determined.[37] The final CoMFA
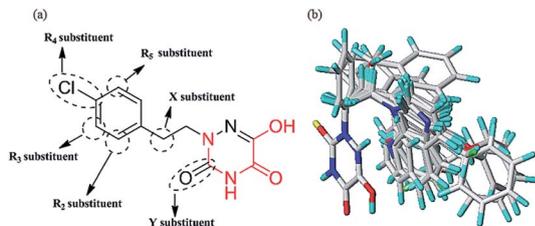
Fig. 2 (a) The common substructure (red) used in database alignment. (b) The alignment result based on the common substructure of compound **13**. Molecules are colored in white for common C, blue for N, red for O, yellow for S, cyan for H, green for F and Cl.

and CoMSIA models of the h-DAAO inhibitors were in accordance with some statistical parameters. Actually, the predictive ability of the models was not completely evaluated with the cross-validated correlation coefficient ($q^2 > 0.5$), the correlation coefficient ($r^2 > 0.9$), ONC value (<10), the standard error of estimate (SEE $\ll 1$) and probability value ($F > 100$).[38] The external validation of both the training and test set is necessary for the reliability of the 3D-QSAR models. In this paper, the root-mean-square error (RMSE) and the mean error measure (MAE) values of the training set were calculated using eqn (1) and (2).[39]

$$\text{RMSE} = \sqrt{\frac{\text{PRESS}}{n}} \qquad (1)$$

$$\text{MAE} = \frac{1}{n}\sum \left| Y_{\text{exp(training)}} - Y_{\text{pred(training)}} \right| \qquad (2)$$

PRESS is the sum of the squared deviations between the actual and predicted biological data for each test set compound, and n is the number of compounds in the training set. The criteria for guaranteeing the accuracy of the 3D-QSAR models include MAE $\leq 0.1 \times$ training set range and MAE $+ 3 \times$ RMSE $\leq 0.2 \times$ training set range.[40] In order to validate the developed models, the external test set of 6 compounds with known activities was predicted, but not applied to the model generation. The predictive correlation coefficient (r_{pred}^2) values, in

reference to eqn (3), were used for judging the quality of the 3D-QSAR model. Herein, SD is the sum of the squared deviations between the pIC_{50} values of the test set and the mean pIC_{50} value of the training set molecules.

$$r_{\text{pred}}^2 = 1 - \frac{\text{PRESS}}{\text{SD}} \qquad (3)$$

Some other external validation parameters R^2, k, R_0^2, R_m^2 and t values are also necessary to evaluate the stability, reliability and predictability of the model. These parameters need to meet certain requirements ($R^2 > 0.6$, $R_m^2 > 0.5$, $0.85 \leq k \leq 1.15$, $t < 0.1$) when the model has good external predictability. They were calculated by the following eqn (4)–(8).

$$R = \frac{\sum \left(Y_{\text{exp(test)}} - \overline{Y}_{\text{exp(test)}} \right)\left(Y_{\text{pred(test)}} - \overline{Y}_{\text{pred(test)}} \right)}{\sqrt{\sum \left(Y_{\text{exp(test)}} - \overline{Y}_{\text{exp(test)}} \right)^2 \sum \left(Y_{\text{pred(test)}} - \overline{Y}_{\text{pred(test)}} \right)^2}} \qquad (4)$$

$$k = \frac{\sum \left(Y_{\text{exp(test)}} \times Y_{\text{pred(test)}} \right)}{\sum Y_{\text{pred(test)}}^2} \qquad (5)$$

$$R_0^2 = 1 - \frac{\sum \left(Y_{\text{pred(test)}} - k \times Y_{\text{pred(test)}} \right)^2}{\sum \left(Y_{\text{pred(test)}} - \overline{Y}_{\text{pred(test)}} \right)^2} \qquad (6)$$

$$R_m^2 = R^2 \left(1 - \sqrt{\left| R^2 - R_0^2 \right|} \right) \qquad (7)$$

$$t = \left| R^2 - R_0^2 \right| / R^2 \qquad (8)$$

where Y_{exp}, Y_{pred} and $\overline{Y}$ are the experimental, predicted and mean activities of the compounds in the test set, respectively.

Molecular docking

Docking and scoring technologies contribute to predicting the binding mode of a bioactive ligand at the active site of the protein in the drug discovery process.[41] Herein, the Surflex-Dock program was used to investigate the most appropriate conformation. The crystal structure of h-DAAO inhibitor was

Table 2 Statistical results of ten different combinations for CoMSIA models

| Combinations | q^2 | ONC | r^2 | SEE | F | r_{pred}^2 | Field contribution (%) | | | | |
							S	E	H	D	A
CoMSIA											
S + E	0.666	7	0.936	0.203	48.159	0.496	0.606	0.394	—	—	—
S + D	0.663	5	0.936	0.194	73.688	0.409	0.971	—	—	0.029	—
S + E + H	0.671	8	0.983	0.108	156.330	0.638	0.205	0.304	0.492	—	—
S + E + D	0.668	9	0.994	0.092	87.329	0.576	0.832	0.150	—	0.018	—
S + E + A	0.685	8	0.956	0.172	59.929	0.507	0.544	0.364	—	—	0.092
S + D + A	0.667	4	0.936	0.192	94.518	0.531	0.834	—	—	0.046	0.120
S + E + H + D	0.659	8	0.985	0.101	178.371	0.658	0.193	0.290	0.488	0.029	—
S + E + H + A	0.646	8	0.985	0.102	175.012	0.643	0.202	0.296	0.460	—	0.042
S + E + D + A	0.700	8	0.955	0.175	58.090	0.531	0.536	0.358	—	0.013	0.092
S + E + H + D + A	0.669	8	0.985	0.100	181.447	0.869	0.192	0.284	0.456	0.029	0.039
Constraints	>0.5	<10	>0.9	$\ll 1$	>100	>0.5	—	—	—	—	—

downloaded from the Protein Data Bank (PDB code: 3W4K). It was essential to do preparatory work on the protein before using the docking programs. Firstly, all water molecules were removed from the original 3W4K protein complex. The side chains and termini chains were repaired after analyzing the protein. The hydrogen atoms and the essential charges were then added to the protein and the protonation type and designated the atom types of the ligand were set. Afterwards, the ProtoMol file was generated by the ligand-based docking mode and each structure was semi-flexibly docked into the active pocket and yielded docking scores. The docking scoring function could be used for predicting the binding affinity between the ligand and the target protein. Finally, each compound could obtain ten different conformations. Taking into consideration the similarity of the orientation between the original ligand and the conformations, the conformation with highest docking score was chosen for the study of the binding mode and molecular dynamics simulation. Meanwhile, to check the accuracy and rationality of the docking method, the root-mean-square deviation (RMSD) value between the docked conformation and the crystal conformation was calculated.

Molecular dynamics (MD) simulation

MD simulations were carried out using the Amber 14.0 software. In the tleap module, the ff14SB force field and the typically general amber force field (gaff) were used for h-DAAO protein and ligands, respectively. The topology file of the ligand-protein structure was generated and the complex was simulated in a hexahedral TIP3P water box of size 78 Å $\times$ 78 Å $\times$ 78 Å. The distance between the border of the solvent box and protein was set to be larger than 8.5 nm. The total charge of the system was then neutralized by the addition of Na^+. All MD simulations followed the procedures for minimization, heating, equilibration and production. Firstly, the energy minimizations of the entire system were divided into two steps. With a constraint force of 100 kcal mol^{-1} $Å^{-2}$, the waters and Na^+ were minimized by 500 steps of the steepest descent method and 500 steps of the conjugate gradient method. The whole system was then minimized by 5000 steps of the descent method, followed by 5000 steps of the conjugate gradient method. Secondly, the system temperature was heated from 0 to 300 K over 50 ps in the NVT ensemble. The systems were then equilibrated in the NPT ensemble at 300 K and 1 atm. A Langevin thermostat was used for temperature control and the SHAKE algorithm was applied to all bonds. Finally, a 10 ns production run was conducted. Trajectories were recorded for each 1 ps, and the last frame was chosen out of 1000 structures for the MD runs.

The stable molecule conformation obtained from MD simulations was used for the binding free energy calculations. In this process, the Molecular Mechanics/Generalized Born Surface Area (MM/GBSA) method was used and the binding free energy (ΔG_{bind}) was calculated using the following equation.

$$\Delta G_{bind} = \Delta G_{complex} - \Delta G_{protein} - \Delta G_{ligand} \approx \Delta G_{gas} + \Delta G_{sol} - T\Delta S$$

$$\Delta G_{gas} = \Delta E_{ELE} + \Delta E_{VDW}; \ \Delta G_{sol} = \Delta G_{GB} + \Delta G_{SA}$$

where ΔG_{gas} is the interaction energy between the protein and ligand in the gas phase. It consists of ΔE_{ELE} (electrostatic energy) and ΔE_{VDW} (van der Waals energy). ΔG_{sol} is the sum of ΔG_{GB} (polar solvation energy) and ΔG_{SA} (non-polar solvation energy). $T\Delta S$ (conformation entropy) is ignored because of its heavy computational cost and weak influence. The above energy parameters were calculated by using the conformations extracted from the last 2 ns.

ADME and bioavailability prediction

In the drug discovery process, the assessments of bioavailability and pharmacokinetics become more important. The predictive models *via* the new SwissADME web tool[42] are necessary and crucial for bioavailability and pharmacokinetics. In particular, when the candidate compounds are many, the computational modeling method is a good choice. In order to evaluate the bioavailability and pharmacokinetics of our newly designed h-DAAO inhibitors, the SwissADME web tool was adopted through the website http://www.swissadme.ch. Firstly, the 2D chemical structures of compounds were drawn in the molecular sketcher and then they were transferred to the SMILES list by clicking on the double-arrow button. Finally, the SMILES list was submitted, and the prediction for bioavailability and pharmacokinetics was calculated after clicking the "Run" button. This study can support the drug discovery efforts in computational chemistry. Specifically, the analysis of bioavailability involves lipophilicity, size, polarity, solubility, saturation and flexibility. These properties were well measured in terms of log P (octanol–water partition coefficient), MW (molecular weight), TPSA (topological polar surface area), log S, fraction C-sp^3 and the number of rotatable bonds, respectively. In addition, the absorption, distribution, metabolism, and excretion (ADME) properties *in vivo* were predicted with the BOILED-Egg model,[42] including human gastrointestinal absorption (HIA), blood–brain barrier (BBB) permeation, cytochrome P450-1A2 (CYP1A2) enzyme inhibition and skin permeation (log K_p). Therefore, ADME and bioavailability predictions are very important for QSAR studies in the process of new drug design, and could be used to further screen out some designed compounds as potent new-type h-DAAO inhibitors.

Overall working process

In this work, we use CoMFA and CoMSIA methodologies to establish the appropriate models, and get the structure–activity relationships (SAR) information. On this basis, we further designed several new compounds and predicted their activities. Also, these compounds were analyzed in detail by molecular docking and molecular dynamics simulations, for directing the synthesis of higher bioactive h-DAAO inhibitors in the future. Simultaneously, the molecular computer-aided design procedure (MOLCAD) was carried out to further validate the 3D-QSAR model and the binding mode in the ligand–protein structure. Finally, three new designed compounds with higher efficiency were selected to predict the pharmacokinetics and bioavailability properties. Our work is presented in a flowchart in Fig. 3S.†

Results and discussions

3D-QSAR statistical results

Table 3 summarizes the statistical results of the 3D-QSAR models. The CoMFA model gave a q^2 value of 0.613 with an ONC value of 6, r^2 of 0.966, SEE of 0.144, and F-statistic value of 115.001. The contributions of the fields were 57.8% of the steric field and 42.2% of the electrostatic field descriptor. The CoMSIA model, obtaining a satisfactory q^2 of 0.669 with an ONC value of 8, r^2 of 0.985, SEE of 0.100, and F value of 181.447, was used for further study. The corresponding field contributions were 19.2%, 28.4%, 45.6%, 2.9% and 3.9% for steric, electrostatic, hydrophobic, hydrogen bond donor, and hydrogen bond acceptor fields, respectively. Comparatively, it was found that the steric, electrostatic and hydrophobic fields played important roles in the optimal CoMSIA model.

The two models had a statistically significant effect on the capability in predicting the activity. Fig. 3 indicates that the actual and predicted activities of the training and test set molecules had strong linear correlations. Furthermore, the high external predictability of the models was reflected in the external validation parameters. For the external validation of the training set, the CoMFA model gave a satisfactory MAE of 0.088, with RMSE value of 0.127, and the MAE and RMSE values of the CoMSIA model were 0.061 and 0.085, respectively. They both obey their corresponding constraints in Table 3. The r_{pred}^2 values of the CoMFA and CoMSIA model were 0.698 and 0.659, respectively, indicating the good external predictive capacity of the models. During the external validation process, the CoMFA model took good values of R^2, k, R_m^2 and t, at 0.894, 0.995, 0.565 and 0.095, respectively. For the optimal CoMSIA model, the
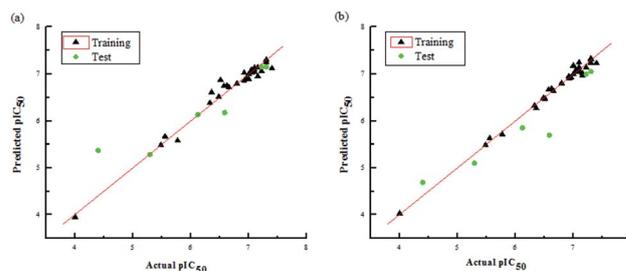

Fig. 3 Plots of actual pIC$_{50}$ values against predicted pIC$_{50}$ values for the data set in the optimal CoMFA (a) and CoMSIA (b) models.
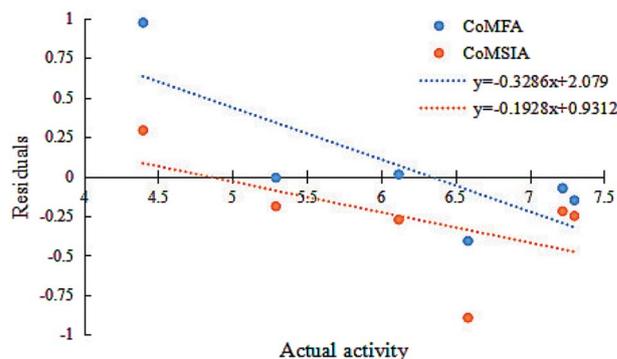

Fig. 4 Residuals vs. activity plots for the random distribution of prediction errors in CoMFA and CoMSIA models.

external validation R^2, k, R_m^2 and t statistics were 0.900, 1.045, 0.812 and 0.010, respectively. In addition, the prediction errors of 3D-QSAR models in the form of a residual plot are clear at a glance in Fig. 4. It was found that the residual values of the test set were randomly distributed around zero; thus, the 3D-QSAR models had good predictability and reliability.

3D-QSAR contour map analysis

To facilitate understanding the effects of fields on activity in a structure-based manner, contour maps (Fig. 5–8) observed from CoMFA (a) and CoMSIA (b) were discussed by showing the regions in which the energy variations of the molecular fields were consistent with changes in bioactivity. The most active compound **13** was used as a reference structure to illustrate all contour maps of the optimal models. This offered insights into the key structural features for potent h-DAAO inhibitors. A default value of 80% contribution for favored regions was defined to visualize the contour maps, while the disfavored regions were 20%. For the steric contour maps, Fig. 5 offers important information on the spatial volume of groups substituted in different positions. The green contour maps mean that the bulky groups were beneficial for improving activity, while the yellow contour maps mean the bulky substituents were disfavored. It should be noted that the steric and electrostatic contour maps obtained from CoMFA were similar to these from CoMSIA. The CoMSIA model showed better predictability, so the contour maps of CoMSIA were used

Table 3 The statistical results for the CoMFA and CoMSIA models

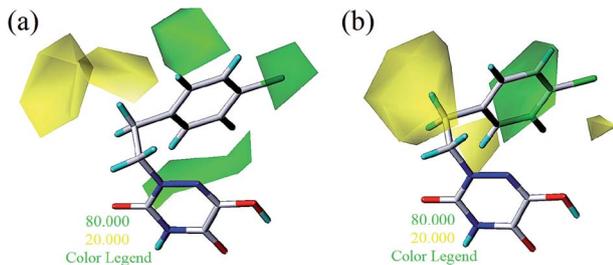| Parameters	CoMFA	CoMSIA	Constraints
MAE	0.088	0.061	$\leq 0.1 \times$ training set range
RMSE	0.127	0.085	MAE $+ 3 \times$ RMSE $\leq 0.2 \times$ training set range
Training set range	3.398	3.398	—
q^2	0.613	0.669	>0.5
ONC	6	8	—
r^2	0.966	0.985	>0.9
SEE	0.144	0.100	$\ll 1$
F	115.001	181.447	>100
r_{pred}^2	0.864	0.869	>0.5
R^2	0.894	0.900	>0.6
k	0.995	1.045	$0.85 \leq k \leq 1.15$
R_0^2	0.988	0.909	—
R_m^2	0.565	0.812	>0.5
t	0.095	0.010	<0.1
Field contribution (%)			
Steric	0.578	0.192	—
Electrostatic	0.422	0.284	—
Hydrophobic	—	0.456	—
H-donor	—	0.029	—
H-acceptor	—	0.039	—

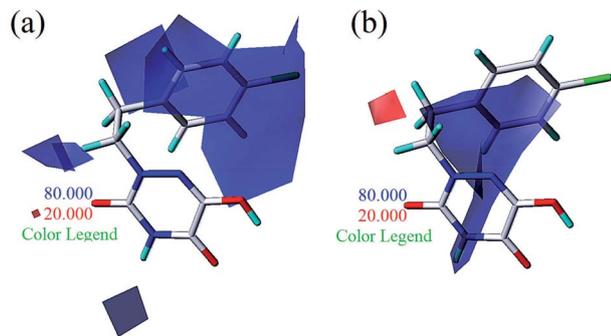**Fig. 5** Steric contours of CoMFA (a) and CoMSIA (b) based on compound **13**.

Fig. 6 Electrostatic contours of CoMFA (a) and CoMSIA (b) based on compound **13**.

to analyze the biological data. A green contour map covering the R_4 position indicated that a bulky group in this region generally got good biological activity. This was in good agreement with the experimental data. For example, **27** ($R_4 = Ph$) > **18** ($R_4 = CF_3$) > **16** ($R_4 = CH_3$) > **24** ($R_4 = OH$). There was a yellow contour map located in the position of X, indicating that compounds with bulky groups were not beneficial for inhibitory activity, as observed from **28** ($X = CH_3$) < **29** ($X = OH$) < **31** ($X = H$).

Fig. 6a and b show the electrostatic field contour maps in CoMFA and CoMSIA analysis, respectively. These contour maps are shown in red (electronegative groups were favorable) and blue (electropositive groups were favorable). A red contour map was nearest to the X position, indicating that having negative electrostatic substituents here was important for increasing the activity. The result also reflected the fact that compound **29** with
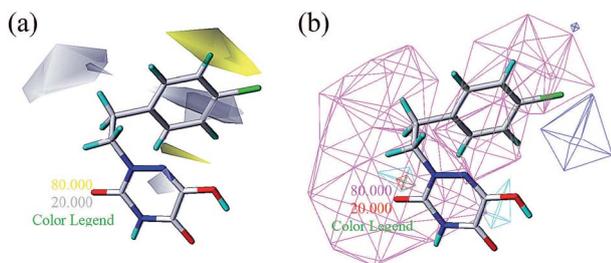

Fig. 8 Steric contours of CoMSIA (a) and CoMFA (b) models. (Blue: compound **4**; red: compound **5**; magenta: compound **6**).

X being a hydroxyl group obviously got better bioactivity than compound **28**. One large blue contour appearing over the position of R_3 illustrated that this region was suitable for improving the electropositivity. Therefore, the biological activity of compound **15** with a methyl substituent was significantly improved compared with compound **23**. The substitutions of observed positions were also used to speed up the structural optimization.

From Table 3, the hydrophobic field (H) was considered to be the most important for the contributions in the developed CoMSIA model. It made a significant contribution to the activity, compared to the other four (S, E, D and A) fields. As shown in Fig. 7a, there was one large white (hydrophilic favorable) contour map around the R_3 and X positions, suggesting that the introduction of hydrophilic moieties into these positions would be of benefit to biological activity. This was consistent with the actual data: **23** ($R_3 = OH$) > **25** ($R_3 = OPh$), **10** ($R_3 = H$) > **17** ($R_3 = CF_3$), **29** ($X = OH$) > **28** ($X = CH_3$). A small white contour map was in the proximity of the 1 N atom of the 1,2,4-triazine structure, indicating that the hydrophilic moieties had little effect on the inhibitory activity. Since the other small white contour maps were far from compound **13**, the analysis of the map was ignored.

One medium-sized yellow (hydrophobic favorable) contour map was located at R_5, indicating that the presence of higher hydrophobic groups at R_5, may be more suitable. At the same time, this yellow contour map was close to R_4, suggesting that hydrophobic groups could improve the inhibitory activity; *e.g.*,

Fig. 7 Hydrophobic contours (a) and hydrogen bonding contours (b) of CoMSIA based on compound **13**. Hydrogen bonding contours include H-bond donors and H-bond acceptors (displayed as lines).
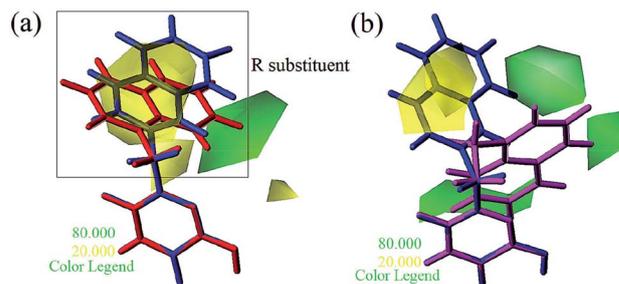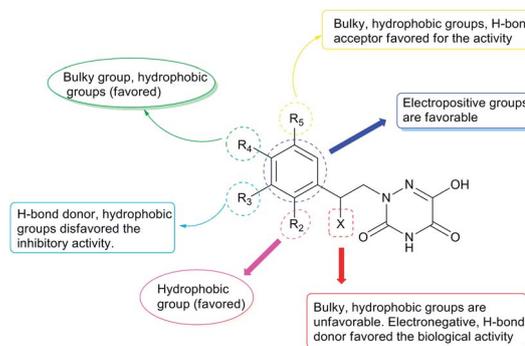

Fig. 9 Structure–activity relationship (SAR) information obtained from 3D-QSAR studies.

Table 4 Structures and predicted pIC_{50} activity, log P and log S values of newly designed h–DAAO inhibitors

No.	Structure	Predicted (pIC_{50})		log P	log S	Surflex-Dock (score)
		CoMFA	CoMSIA			
13		7.118	7.228	1.55	−3.00	6.9737
D1		7.845	7.593	1.03	−2.80	8.4487
D2		7.513	7.689	1.53	−3.38	8.9393
D3		7.878	7.787	2.18	−3.57	8.2162
D4		7.851	7.720	2.34	−3.69	7.6383
D5		7.823	7.729	2.71	−4.10	7.9024
D6		7.813	7.751	2.96	−4.51	7.3262
D7		7.711	7.663	2.90	−4.50	9.0727
D8		7.723	7.820	1.99	−3.13	8.2472
D9		7.638	7.853	2.68	−4.06	9.3982

13 (R_4 = Cl) > **10** (R_4 = H) > **24** (R_4 = OH). A small yellow contour map near R_2 showed that the hydrophobic moieties were favorable. This agreed well with actual data: **14** (R_2 = F) > **22** (R_2 = OH). In Fig. 7b, the hydrogen bond donor and acceptor contour maps are displayed as lines. The purple color means that groups with a hydrogen bond donor were disfavored and the cyan color means that hydrogen bond donors were favored. On the contrary, the large magenta color contour indicated that the activity of compounds with a hydrogen bond acceptor, like compound **30** (Y = S), Test 5 (R_3 = F), Test 6 (R_4 = F), increased as compared with compound **10**.

Apart from the compounds discussed above, two compounds **5** and **6** with bulky naphthalene moieties showed good inhibitory activities, even greater than the similar compound **4**. As displayed in Fig. 8a, a yellow contour around the R substituent indicated that steric hindrance disfavored the activity. However, another green contour was located in the naphthalene moiety of compound **5**. This is a possible reason why compound **5** (pIC_{50} = 7.301) was more potent than compound **4** (pIC_{50} = 6.658). From Fig. 8b, a yellow contour and three green contours appeared on the R groups of compounds **4** and **6**, respectively. This meant that the bulky group of compound **6** would increase the activity. This result was supported by the activity order of **6** > **4**.

Design of new compounds with higher inhibitory activity

Based on the above comprehensive analysis of contour maps, the SAR information revealed by 3D-QSAR is illustrated in Fig. 9, which could guide the design of new compounds with high bioactivity. We designed a tot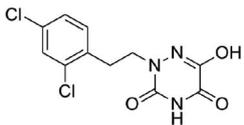al of 9 compounds using compou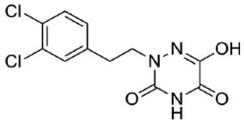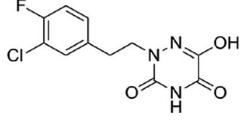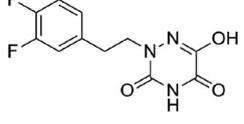nd **13** (which had the highest activity) as a reference molecule, and their solubility (log S) and lipophilicity (log P) were predicted using the SwissADME web tool[42] in Table 4. The modified parts are mainly focused on three substituents (R_2, R_4 and R_5). Since the bulky groups are favored for the activity at the R_5 position, pyrazolyl was introduced in this position to yield compound **D1**. The previous contour maps suggested that some bulky substituents (ethyl, cyclopropyl, cyclobutyl, cyclopentyl and phenyl group) would improve the activity on the R_4 position. Also, considering the advantages of hydrophobicity on the R_2 position, the compounds **D3**, **D4**, **D5**, **D6** and **D7** were designed. Due to the fact that the introduction of fluorine can increase the liposolubility of drugs, compounds **D8** and **D9** were designed. Additionally, considering the advantageous conditions of R_4 and R_5 with a comprehensive understanding, compound **D2** was obtained. Most of the compounds were designed according to steric and hydrophobic fields. Table 4 indicates that they had reasonable absorbency and solubility. In short, it was found that compounds **D1**, **D3** and **D8** showed higher inhibitory activity than other compounds.

Research has shown that the introduction of halogen and alkyl groups into the aromatic ring should increase the efficacy of compounds theoretically, since these groups can respectively improve lipid solubility and chemical stability.[43,44] Also, the introduction of naphthenic base can heighten the effectiveness of medications by enhancing both lipid solubility and chemical stability. The introduction of pyrazolyl can improve inhibitory activity by forming hydrogen-bonding interactions with receptors. This is consistent with computational modeling analysis, and the evidence strongly supports that **D1** (R_5 = pyrazolyl), **D3** (R_4 = ethyl), **D4** (R_4 = cyclopropyl) and **D8** (R_2 = F) have better biological activities than compound **13**.

Practical application and evaluation of the 3D-QSAR model

Some h-DAAO inhibitors with different structures were reported by Tsukamoto *et al.*[45] Among these were another four compounds (**5y**, **10b**, **5z**, **5m**) based on the 6-hydroxy-1,2,4-triazine-3,5(2H,4H)-dione scaffold, which act as h-DAAO inhibitors, as shown in Table 5. The biological activity of compound **5y** was higher than that of template compound **13**. Furthermore, the activities of these four compounds could be explained well by the SAR information obtained from the 3D-QSAR model. The introduction of hydrophobic groups at the R_4-position could improve the inhibitory activity as shown in Fig. 9; *e.g.*, **5y** (R_4 = Cl) > **12** (R_4 = H), **10b** (R_4 = F) > Test 5 (R_4 = H). Similarly, the activity of compound **5z** (R_3 = Cl) was lower than that of compound Test 6 (R_3 = H) due to the fact that the hydrophobic groups disfavored the inhibitory activity at the R_3 position. Compound **5m** exerted higher activity compared to compound **11** because the addition of Cl at the R_4-position not only increased the steric field but also increased hydrophobicity, which contributed to the increasing activity and made all the sense in Fig. 9. We could therefore conclude that the SAR information obtained from the 3D-QSAR model could indicate the directions of the compound modification and save lots of manpower, material resources and research time.

Table 5 Structures and actual pIC_{50} activity values of four new h-DAAO inhibitors, compared with their predicted activities by CoMFA and CoMSIA models

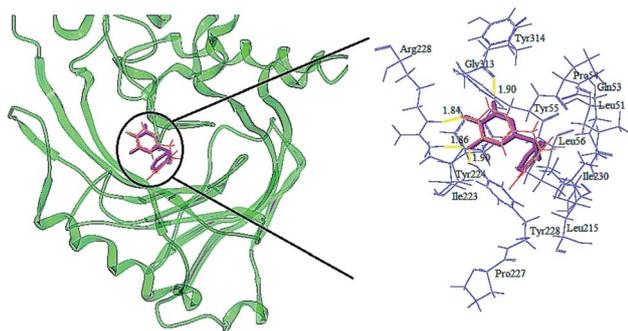| No.	Structure	Actual pIC_{50}	Predicted pIC_{50}	
			CoMFA	CoMSIA
5m		7.097	7.262	7.676
5y		7.523	7.259	7.619
5z		7.222	7.072	7.481
10b		7.398	7.234	7.407

Fig. 10 Re-docking of the compound into the binding site of h-DAAO (3W4K). Hydrogen bonds are shown as yellow lines, with distance unit of Å (magenta: the re-docked ligand; red: the original ligand).

In this work, our 3D-QSAR model was used to predict the activities of these four compounds and the inhibitory activities are also listed in Table 5. The results showed that the predicted activity values were close to their experimental values, indicating that our model had good predictability, reliability and practical significance. However, only the activity of compound **5y** was higher than that of the template compound **13** in these four compounds, and it is of great worth to study more efficient h-DAAO inhibitors with 1,2,4-triazine *in silico*. The model was also used to predict the newly designed compounds. On comparing Tables 4 and 5, it was found that the predicted activities of these newly designed compounds were much higher compared to compound **5y** and compound **13**. The findings suggested that the designed compounds had higher

activities and could provide a reliable theoretical basis for the future synthesis of new potent h-DAAO inhibitors. These findings have profound guiding significance for the emergence and development of more efficient antipsychotic drugs.

Molecular docking analysis

Molecular docking is the most extensive program for identifying protein–ligand interactions. The program is effective in simulating the possible binding modes between small molecules and whole protein targets. In the evaluation of docking accuracy, the target ligand was re-docked into the crystal structure of the protein (PDB code: 3W4K). It has been reported that the root mean square deviation (RMSD) value should be less than 2.0.[46] In this study, the corresponding RMSD and similarity of the re-docking result were 0.379 and 0.862, respectively, which indicated that the docking method was rational; the re-docking result is illustrated in Fig. 10. Although there was a small rotation angle, it was found that the re-docking structure and the original structure possessed the same binding site. It could also be seen that some key amino acids (Arg283, Gly313, Tyr224 and Tyr228) that interacted with the inhibitor at the binding site were consistent with existing reports. The compound was docked in the binding site *via* three hydrogen bonds and one π–π interaction. The key residues Arg283 and Tyr228 interacted with the inhibitor by hydrogen bonding. The hydrogen bond distances observed were 1.87 Å (Arg283–NH⋯OH), 1.97 Å (Arg283–NH⋯O=), and 2.40 Å (Tyr228–HO⋯HO). The π–π interaction was observed between Tyr224 and the triazine ring. It was concluded that the Surflex-Dock docking method and the
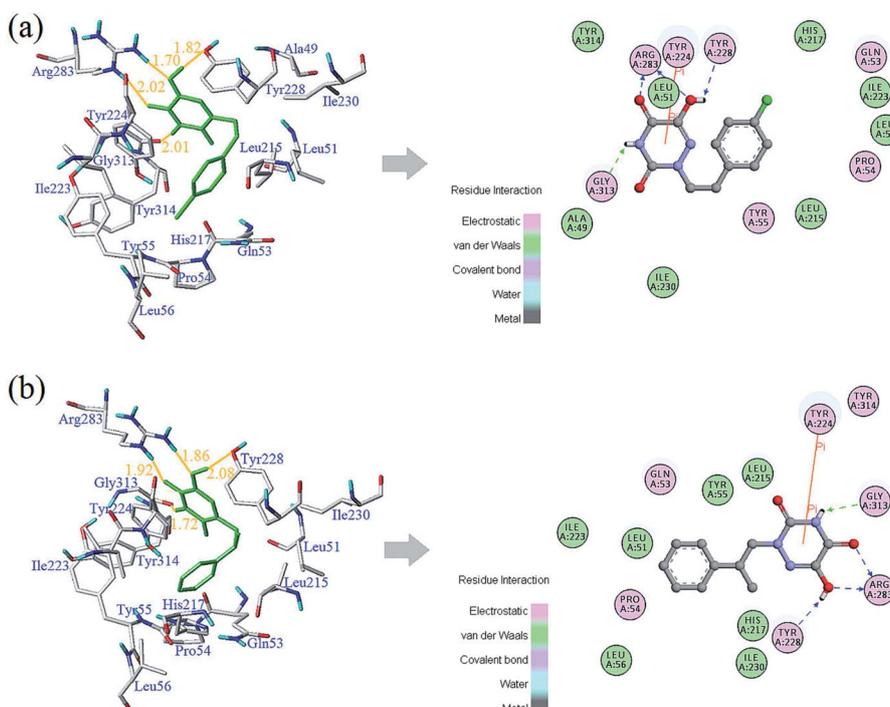

Fig. 11 Docking results and 2D maps of the selected compounds **13** (a) and **28** (b) in the binding site of the protein (PDB entry code: 3W4K). The inhibitor and the key residues are shown as stick models. Hydrogen bonds are described as yellow lines, with distance in Å units.
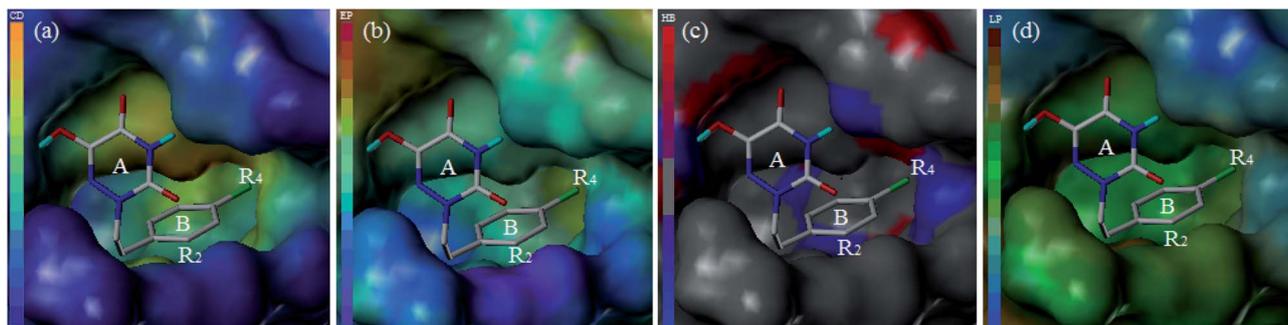
Fig. 12 MOLCAD surface displayed by cavity depth (a), electrostatic potential (b), hydrogen bonding sites (c) and lipophilic potential (d) for compound **13** at the active site of h-DAAO.

re-docking results were reasonable and reliable, and Surflex-Dock was subsequently used for docking. Firstly, all compounds were docked into the binding pocket of the protein to explore the binding mode (Fig. 4S†), and hydrogen bond interactions were formed between the 1,2,4-triazine derivatives and several key residues, including Ala49, Leu50, His217, Tyr224, Tyr228, Arg283 and Gly313. The binding pocket of the protein is shown in Fig. 5S,† as well as the binding mode of compounds **4**, **5** and **6**. The geometry of the pocket looks like a "cave" and the three molecules were semi-flexibly docked onto the active pocket. Compound **5** had one residue more than compounds **4** and **6**. Furthermore, the hydrogen bond interaction between molecule **4** and the protein was weaker compared to compounds **5** and **6**, indicating that hydrogen bond interactions played an important role in the activity. It was found that the activity order was **5** > **6** > **4**. These observations are in agreement with the analysis of the 3D-QSAR contour maps.

The detailed analyses of two molecules (**13** and **28**) are displayed in Fig. 11. Compound **13** was docked in the binding site *via* four H-bonds and one π–π interaction. The key residues Arg283, Tyr228 and Gly313 interacted with the inhibitor by H-bond. The H-bond distances were observed to be 1.70 Å (Arg283–NH⋯OH), 2.02 Å (Arg283–NH⋯O=), 1.82 Å (Tyr228–HO⋯HO) and 2.01 Å (Gly313=O⋯H–N). The 5-O group of the triazine ring formed one H-bond with the protein, consistent

with the contour maps of CoMSIA as shown in Fig. 7b, where the 5-position group was found favorable as a H-bond acceptor. Also, two H-bonds of the 6-OH group matched the H-bond donor map of the 3D-QSAR model. The π–π interaction was observed between Tyr224 and the triazine ring. These two interactions were similar to the results in literature.[25]

It was shown that the triazine ring was important for the activity of h-DAAO inhibitors, and agreed well with the high bioactivities of many triazine derivatives. In addition, electrostatic and van der Waals interactions were formed between the compound and several residues in the 2D maps obtained from Discovery Studio 4.5. The hydrophobic acting force had the greatest effects on bioactivity from the analysis results of CoMSIA and it was found that there were hydrophobic interactions with Leu51, His217, Gln53, Leu215, Arg283, Tyr224, Tyr228 and Gly313 residues located in the hydrophobic pocket. The binding mode of compound **13** indicated that eight residues Arg283, Tyr224, Tyr228, Leu51, His217, Gln53, Leu215 and Gly313 were necessary for interacting with h-DAAO inhibitors, and H-bonds and hydrophobic interactions were very important factors in improving the inhibitory activity.

The interactions between compound **28** and the active site are depicted in Fig. 11b. The ligand was docked into the binding site *via* four hydrogen bonds and one π–π interaction. The hydrogen bond distances observed were 1.86 Å (Arg283–NH⋯
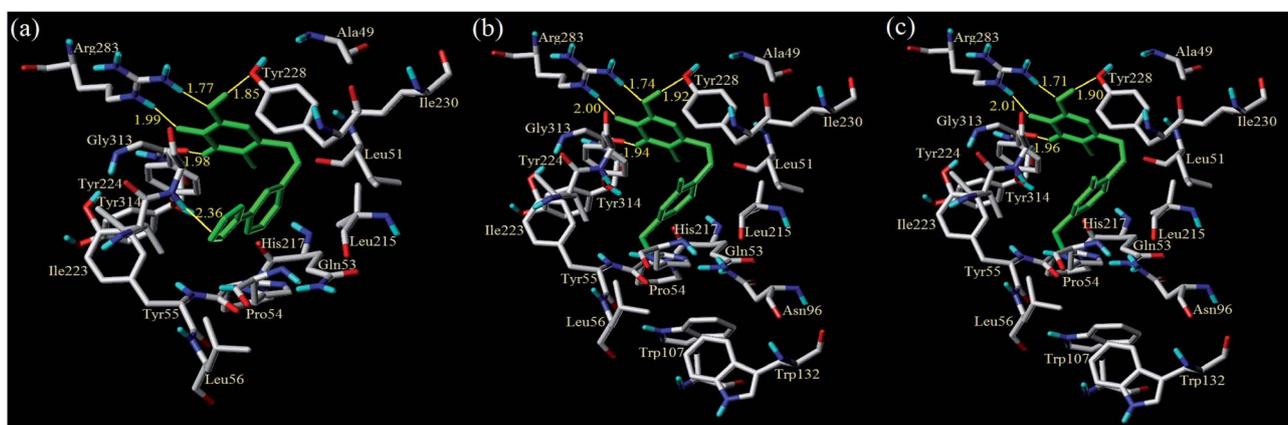

Fig. 13 Docking results of the designed compounds **D1** (a), **D3** (b) and **D8** (c) in the binding sites of protein 3W4K (yellow lines: hydrogen bonds).

OH), 1.92 Å (Arg283–NH⋯O═), 2.08 Å (Tyr228–HO⋯HO) and 1.72 Å (Gly313═O⋯H–N). The π–π interactions were also observed between Tyr224 and the triazine ring. Some residues (such as Leu51, Leu56, Leu215, Ile223, Ile230, His217, Tyr55 and Pro54) formed van der Waals interactions with the target molecule. Some other residues, including Arg283, Gln53, Gly313, Tyr224 and Tyr228, formed electrostatic interactions. Compound **28** had the same hydrophobic residues as compound **13**, but compound **13** had one more amino acid residue (Ala49) than compound **28**. The residue Ala49 could interact with the compound *via* electrostatic and hydrophobic interactions, which affected the bioactivity of h-DAAO inhibitors from the field distributions in the CoMSIA model. This is the reason compound **13** had better activity than compound **28**.

According to the docking results of all compounds, the key h-DAAO residues in the docking pockets of the protein (3W4K) were found to be Gly313, Arg283, Tyr224, Tyr228 and Leu51. To obtain new compounds with higher efficiency, the triazine structure has to be maintained. The substituents (type and position) on the benzene ring of the inhibitors can then be modified, aiming to form hydrophobic interactions with acid residues (His217, Leu215, Leu51) for stabilizing the ligand in the active site. In terms of increasing the activity of the h-DAAO inhibitors, it is vital to do modifications with some suitable substituents. Therefore, the binding mode was complementary to the CoMFA and CoMSIA models.

For the sake of further verification of the binding mode and 3D-QSAR models, the MOLCAD surface with compound **13** was determined (Fig. 12). MOLCAD computed and displayed four surface properties, namely, cavity depth (CD), electrostatic potential (EP), hydrogen bonding sites (HB) and lipophilic potential (LP). As shown in Fig. 12b, the color ramp on the left representing the surface of the EP ranges from red (positive) to purple (negative). The entire ring B, especially in the R_2 position, was immersed in the purple area and without any red color on the surface, so the introduction of electropositive substituents into ring B was favored for the activity. In addition, the color ramp of HB is from red (H-bond donor) to blue (H-bond acceptor) in Fig. 12c. Therefore, the R_4 substituent on ring B was oriented towards the red surface, indicating that it is advantageous to use hydrogen bond acceptor groups as R_4 substituents. The color ramp also represents the hydrophobic degree of surface changes from hydrophobic (brown) to hydrophilic (blue). Thus, the area near the R_4 substituent was light brown in Fig. 12d, suggesting that hydrophobic groups at the R_4 position could increase the activity. All of the above conclusions are well in agreement with the SAR information obtained from 3D-QSAR studies, which also verified the correctness of the docking pocket. Finally, it can be concluded that the MOLCAD surface maps at the active site were highly consistent with the 3D-QSAR model in terms of hydrogen bonding, electrostatic and hydrophobic potentials.

After the compounds with known activities were docked into protein h-DAAO, the docking with all designed molecules was studied, shown in Fig. 6S.† The docking results illustrated that most of the designed compounds (*i.e.*, **D1**, **D2**, **D3**, **D7**, **D8** and **D9**) had higher docking scores, and the orientation of the
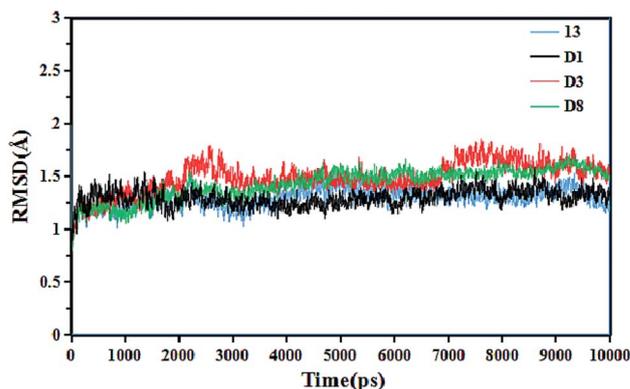

Fig. 14 Root-mean-square deviation (RMSD) of the ligand–3W4K complexes *versus* the dynamics simulation time.

molecules was similar to the original ligand. Moreover, several residues, Tyr224, Gly313, Arg283, Ala49, Gly50 and Tyr228, interacted with the binding pocket, mainly through H-bonds with the triazine ring. This indicated that the H-bond interaction in the triazine region was beneficial for binding affinity and activity.

From Table 4, compounds **D1**, **D3** and **D8** had higher predicted pIC_{50} values and docking scores among the newly designed molecules, so they were further studied for in-depth analysis. As shown in Fig. 13, compound **D1** docked into the cave-like pocket *via* five H-bonds and one π–π interaction. The 4,5,6-positions of the triazine ring formed four H-bonds with the amino acids Gly313, Arg283 and Tyr228, respectively. Another H-bond interaction was found between the pyrazolyl region and residue Tyr224 at distance of 2.36 Å. Additionally, the electrostatic and van der Waals interactions of **D1** were similar to molecule **13**. The strengthened H-bonds of **D1** were helpful for the binding affinity, which obviously enhanced h-DAAO inhibitory activity. For compound **D3**, the H-bond distances were observed to be 1.74 Å (Arg283–NH⋯OH), 2.00 Å (Arg283–NH⋯O═), 1.92 Å (Tyr228–HO⋯HO), and 1.94 Å (Gly313═O⋯H–N), respectively. For compound **D8**, the H-bond distances were 1.71 Å (Arg283–NH⋯OH), 2.01 Å (Arg283–NH⋯O═), 1.90 Å (Tyr228–HO⋯HO), and 1.96 Å (Gly313═O⋯H–N), respectively. One π–π interaction was still observed between Tyr224 and the triazine ring. Some residues were used to form electrostatic interactions. Moreover, the other eight residues, such as Leu215, His217, Leu51, Tyr228, Arg283, Gly313, Tyr224 and Gln53, had the important hydrophobic interactions at the hydrophobic pocket. These interactions were the same as with compound **13**. Some of the amino acids surrounding R_2, R_4 and R_5 of the benzene ring were hydrophobic, declaring that the hydrophobic substituent at the R_2, R_4 and R_5 positions could increase activity. Hydrophobic amino acids like Pro54, Tyr55, Leu51, Trp107, Ile223 and Ile230 were present in the proximity of R_2, R_4 and R_5, which validated the hydrophobic contour maps of CoMSIA.

There are some significant differences between the newly designed compounds and the template compound **13**. The number of key residues that interacted with the new

Table 6 Binding free energies of inhibitor–protein complexes and the different energy contributions

No.	ΔE_{ELE} (kcal mol^{-1})	ΔE_{VDW} (kcal mol^{-1})	ΔG_{gas} (kcal mol^{-1})	ΔG_{GB} (kcal mol^{-1})	ΔG_{SA} (kcal mol^{-1})	ΔG_{sol} (kcal mol^{-1})	ΔG_{bind} (kcal mol^{-1})	pIC$_{50}$ (predicted)	Docking score
13	−36.3352	−23.5881	−59.9233	39.8916	−4.6625	35.2291	−24.6943	7.398	6.9737
D1	−40.2932	−26.6170	−66.9102	40.2745	−5.4155	34.8590	−32.0512	7.845	8.4487
D3	−36.9914	−24.3826	−61.3740	37.4548	−4.8269	32.6279	−28.7461	7.787	8.2162
D8	−40.2643	−26.3763	−66.6405	40.1342	−4.8613	35.2729	−31.3676	7.820	8.2472

compounds through van der Waals interactions to stabilize the ligand, like residues Trp107, Trp132 and Asn96, increased significantly. Furthermore, it was noted that the compounds **D1**, **D3** and **D8** had shorter hydrogen bond distances than **13**, which would enhance the binding affinity between the inhibitors and protein. These findings accounted for the order of their inhibitory activities: compound **D3** > **13** > **28**. These were also consistent with the predicted activity in the 3D-QSAR model.

MD simulation analysis

To gain insight into the dynamic interactions between the inhibitors and receptor protein (3W4K), MD simulations were run on our lab's server for four representative inhibitors **13**, **D1**, **D3** and **D8**. The system stability was determined in terms of the root-mean-square deviation (RMSD) of the complex backbone C$_\alpha$ atoms. The plots of the RMSD values *versus* the dynamic simulation time are illustrated in Fig. 14. It was found that all protein–ligand complexes were stable after 6 ns simulations, and the system had good convergence. In addition, the RMSD values fluctuated between 1 Å and 2 Å, indicating that the complexes were close to the native state. Moreover, the plots of total-energy and temperature *versus* time are shown in Fig. 7S.† This trend also indicated that the system had good stability. The

superimposition of the original **13**-3W4K complex and the equilibrium structure after 10 ns simulations are displayed in Fig. 8S.† Except for a small rotational angle, it can be recognized that the two structures are similar, and the original docked structure and the dynamics simulated structure adopted the same binding site of h-DAAO, which further determined the stability of the system and confirmed the reliability of the docking results.

The root mean square fluctuation (RMSF) value reflects the fluctuations in the protein amino acids residues. Fig. 9S† shows the relationship between the RMSF values of the complex backbone C$_\alpha$ atoms and the residue number in four dynamics simulated complexes. It can be seen that the inhibitor-protein complexes **13**-3W4K, **D1**-3W4K, **D3**-3W4K and **D8**-3W4K had similar fluctuations, suggesting that the binding patterns of these inhibitors were similar. In Fig. 9S,† four residues Tyr224, Tyr228, Arg283 and Gly313 were labeled, which could form strong H-bonds interactions with inhibitors. Furthermore, the RMSF values of Tyr224, Tyr228, Arg283 and Gly313 were observed to be 0.3814 Å, 0.3149 Å, 0.3898 Å and 0.4055 Å, respectively. These amino acids residues with lower RMSF values showed rigid behaviours and good stability. Thus, compounds **13**, **D1**, **D3** and **D8** had good binding affinities with h-DAAO.

Based on the MD simulations, MM/GBSA binding free energies for the four inhibitors of the last 2 ns trajectory were calculated in Table 6. It is generally recognized that the binding free energy values of inhibitors with higher activities are more negative. The binding free energies ΔG_{bind} of compounds **13**, **D1**, **D3** and **D8** were −24.6943 kcal mol^{-1}, −32.0512 kcal mol^{-1}, −28.7461 kcal mol^{-1} and −31.3676 kcal mol^{-1}, respectively. This showed that ΔG_{bind} values were in agreement with the predicted pIC$_{50}$ values of the 3D-QSAR model; the corresponding pIC$_{50}$ activity order is **D1** (7.845) > **D8** (7.820) > **D3** (7.787) > **13** (7.398). It can also be seen that the greatest contributors to the whole binding free energy were van der Waals energy ΔE_{VDW}, followed by electrostatic energy ΔE_{ELE}; therefore, ΔE_{VDW} values were the key factors of ΔG_{bind}. In addition, the ΔG_{GB} values are positive, indicating that polar solvation energy is unfavourable for ΔG_{bind}. In contrast, the ΔG_{SA} values are negative, suggesting that non-polar solvation energy is favourable. The ΔG_{bind} values of new compounds are more negative compared to **13**, showing their greater inhibitory activities. From the structural viewpoint, one reason might be the introduction of F, Cl and pyrazolyl into the benzene ring, which could be confirmed by docking.
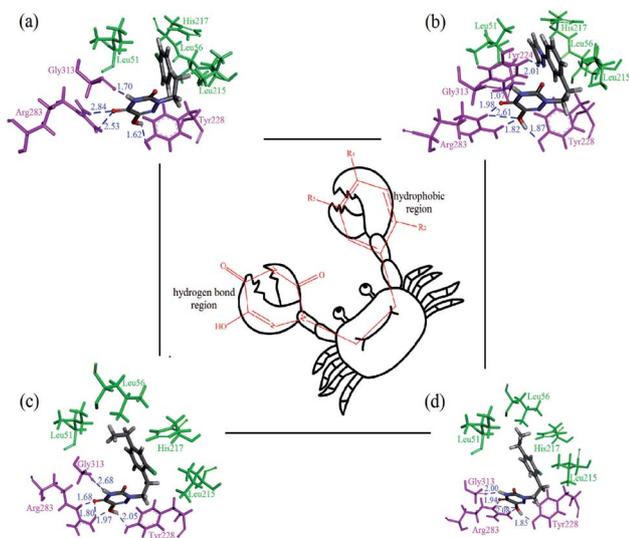

Fig. 15 Docking results of dynamics simulated ligand–3W4K complexes, and the 'crab' conformation of compounds at the binding site of the protein: (a) compound **13**; (b) compound **D1**; (c) compound **D3**; (d) compound **D8** (magenta: H-bond interaction; green: hydrophobic interaction).

Table 7 ADME and bioavailability predictions for newly designed compounds

No.	$\log P$	MW (g mol^{-1})	TPSA (Å^2)	$\log S$	Fraction Csp^3	Num. rotatable bonds	HIA probability	BBB	CYP1A2 inhibition	$\log K_P$ (cm s^{-1})
13	1.55	267.67	87.98	−3.00	0.18	3	High	No	Yes	−6.57
D1	1.03	299.28	87.98	−2.80	0.31	4	High	No	Yes	−6.41
D3	2.18	295.72	87.98	−3.57	0.31	4	High	No	Yes	−6.17
D8	1.99	279.27	87.98	−3.13	0.31	4	High	No	Yes	−6.45
Optimal range	−0.7–5.0	150–500	20–130	≤6	≥0.25	≤9	—	—	—	—

Subsequently, the dynamics stable complexes, **13**-3W4K, **D1**-3W4K, **D3**-3W4K and **D8**-3W4K, were extracted for docking analysis. From the perspective of amino acids, the various interactions between triazine compounds and protein were explored. The designed molecules **D1**, **D3** and **D8** were perfectly docked onto the active site of the h-DAAO protein. The binding patterns were very similar to that of **13**, and the triazine and benzene rings occupied the same position as the corresponding moieties of **13**. The docking results of inhibitor-protein structures are displayed in Fig. 15. It can be seen that van der Waals and electrostatic interactions still existed after MD simulations, but hydrophobic and H-bond interactions became stronger. For the **13**-3W4K complex, the carbonyl group at the 5-position of the triazine ring formed two H-bonds with NH of Arg283, The third H-bond was found between the NH at the 4-position of the triazine ring and the carbonyl of Gly313. Moreover, the OH group at the 6-position of the triazine ring formed H-bond interactions with Tyr228 at a distance of 1.62 Å. The stable H-bond interactions in the triazine ring region were considered to be a key factor for inhibitory activity, and the benzene ring was located in the hydrophobic region, which could be responsible for the good activity of compound **13**. For inhibitors **D1**, **D3** and **D8**, the 4,5,6-positions of the triazine ring formed five H-bonds with amino acids Gly313, Arg283 and Arg228 in the same way. The Cl of R$_2$, ethyl of R$_4$ and pyrazolyl of R$_5$ interacted with the surrounding residues, making the benzene ring closer to the hydrophobic pocket, and the strong hydrophobic interaction favoured the binding stability of **D1**, **D3** and **D8**. Therefore, compared with **13**, the h-DAAO inhibitory activities of **D1**, **D3** and **D8** significantly improved. In short, the introduction of hydrophobic moieties into R$_2$, R$_4$ and R$_5$ of 1,2,4-triazine derivatives is beneficial for inhibitory activity.

The docking results were consistent with CoMFA and CoMSIA analyses. For example, the docking results showed that the ethyl groups of the benzene ring in **D3** and **D8** were helpful in forming stable hydrophobic interactions, which could enhance activity. As shown in Fig. 7a, a yellow contour map appeared on the R$_4$ position of the benzene ring, suggesting that the introduction of hydrophobic groups at this position leads to higher activity. From Fig. 7b, the H-bond contour maps near the triazine ring indicate that strong H-bond interactions would improve the biological activity, and the docking results show that triazine rings formed strong H-bonds with the residues. It is also important to note that **D1**-3W4K not only formed H-bonds with the triazine region, but also formed H-bonds with

the benzene region. Meanwhile, the docking scores of compounds **D1** (8.4487), **D3** (8.2162) and **D8** (8.2472) are obviously higher compared to compound **13** (6.9737). This is inconsistent with the conclusion that **D1**, **D3** and **D8** have more negative binding free energies (stronger binding affinity) than molecule **13** in the MD simulations. These findings can also validate the accuracy of earlier SAR information obtained from 3D-QSAR. In conclusion, the newly designed compounds **D1**, **D3** and **D8** can be used as potential h-DAAO inhibitors.

Based on the results of these computational methods, we assumed the binding mode between inhibitor and protein to be a 'crab' conformation (Fig. 15). Through the comprehensive analysis of compounds **13**, **D1**, **D3** and **D8**, it was found that a C–C single bond formed the 'mouth', and the triazine ring and benzene ring served as the two big 'pincers', respectively. Firstly, the 'mouth' of the 'crab' was bound to the receptor *via* a C–C single bond and X substituent. Secondly, the left 'pincer' interacted with the protein mainly by hydrogen bonds and electrostatic interactions. Some hydrophobic residues (His217, Leu51, Leu56 and Leu215) interacted with the benzene ring, and we could consider the right 'pincer' as the important hydrophobic region. The above analysis shows that the results of CADD for h-DAAO inhibitors were valid. Therefore, we can draw the conclusion that the results of the 3D-QSAR, docking and dynamics simulations were reliable and verified each other.

ADME and bioavailability analysis

In the R&D process for new drugs, ADME and bioavailability analysis played significant roles in drug-likeness. The designed compounds **D1**, **D3** and **D8** with higher predicted activities and good stability were selected for ADME and bioavailability prediction. The ADME parameters calculated by the SwissADME web tool[42] for the representative inhibitors are summarized in Table 7. The results showed that the log P values of the designed compounds **D1**, **D3** and **D8** were 1.03, 2.18 and 1.99, respectively, indicating that they have a reasonable absorbency. Meanwhile, **D1** (log S = −2.80), **D3** (log S = −3.57) and **D8** (log S = −3.13) were considered to have good solubility in the body. The bioavailability radars of these inhibitors were analyzed intuitively in Fig. 10S.† The pink areas meant the optimum range of six properties, namely, lipophilicity, size, polarity, solubility, saturation and flexibility. It was found that compound **13** was outside the pink area, due to the inconformity of saturation. In contrast, the new inhibitors **D1**, **D3** and **D8** had superior bioavailability. In addition, the ADME

descriptors were studied through a BOILED-Egg model (Fig. 11S†). Four compounds all exerted high HIA (in the white region) and the yolk (yellow region) represents the high probability of brain penetration. The new compounds **D1**, **D3** and **D8** were not brain penetrant, the same as compound **13**. However, their $\log K_{\mathrm{p}}$ values were larger than that of compound **13**, indicating that the skin permeability of the designed molecules is better. The "Yes" in Table 6 indicates that the compound has a greater probability of being the inhibitor of CYP1A2. Therefore, the newly designed compounds can be excreted *via* metabolic biotransformation by the inhibition of the cytochrome CYP1A2 enzyme. In short, bioavailability and pharmacokinetics predictions could improve the success rate of newly designed inhibitors. These are also beneficial for obtaining safer and more potent h-DAAO inhibitors for the treatment of schizophrenia.

Conclusion

The structure–activity relationship and binding interactions of 37 novel h-DAAO inhibitors were investigated theoretically and by means of CADD, including 3D-QSAR modelling, molecular docking and molecular dynamics simulation methods. A reliable 3D-QSAR model was established. The model exhibited good predictability and could be employed for predicting more new compounds. The contour maps of the 3D-QSAR revealed that hydrophobic, electrostatic and steric fields played an important role in designing the molecular structure, which was verified and supplemented by the MOLCAD molecular surface. The molecular docking and molecular dynamics studies with the 'crab' conformation revealed that the triazine ring and the substituents (type and position) of the benzene ring greatly affect the inhibitory activity. Meanwhile, the H-bonds that were formed by the 4,5,6-position of triazine with Gly313, Arg283 and Tyr228 were important for activity. The key hydrophobic residues, Leu51, His217, Gln53 and Leu215, were vital elements in the stability of the inhibitor at the binding site. Therefore, to obtain novel h-DAAO inhibitors with high efficiency, the triazine structure should be retained and the modified sections should mainly be in the R_2 and R_4 benzene ring positions with hydrophobic and bulky substituents, respectively. Moreover, to design compounds **D3** and **D8** with high inhibitory activity, chlorine or fluorine was introduced into the R_2 position of the benzene ring, and ethyl was simultaneously set on the R_4 position. **D1** was obtained by the modification of pyrazolyl in the R_5 position. The activities of all the newly designed compounds were superior to those of the published triazine compounds, **5y**, **10b**, **5z** and **5m**, which supports the reliability of the model and the accuracy of the design of the new compounds. These theories provide an understanding of the structural features of h-DAAO inhibitors and their binding interaction with protein, and therefore, the results could provide profound guidance and practical significance for the future design and experimental synthesis of novel h-DAAO inhibitors with high bioactivities. The results also supply great reference values for the emergence and development of new types of safe and effective antipsychotic drugs.

Conflicts of interest

The authors declare that there are no financial/commercial conflicts of interest.

Acknowledgements

References

1 M. Möller, T. Swanepoel and B. H. Harvey, *ACS Chem. Neurosci.*, 2015, **6**, 987–1016.
2 A. G. Awad and L. N. Voruganti, *PharmacoEconomics*, 2008, **26**, 149–162.
3 S. Grover, S. Chakrabarti, N. Hazari and A. Avasthi, *Psychiatry Res.*, 2017, **249**, 349–353.
4 D. S. Berman and J. Davis-Berman, *J. Exp. Educ.*, 2005, **28**, 17–24.
5 L. Orsolini, C. Tomasetti, A. Valchera, R. Vecchiotti, I. Matarazzo, F. Vellante, F. Iasevoli, E. F. Buonaguro, M. Fornaro, A. L. Fiengo, G. Martinotti, M. Mazza, G. Perna, A. Carano, A. De Bartolomeis, M. Di Giannantonio and D. De Berardis, *Expert Opin. Drug Saf.*, 2016, **15**, 1329–1347.
6 A. Abbott, *Nature*, 2010, **468**, 158–159.
7 F. A. Mustafa, J. G. Burke, S. S. Abukmeil, J. J. Scanlon and M. Cox, *Pharmacopsychiatry*, 2015, **48**, 11–14.
8 I. J. Anwar, K. Miyata and A. Zsombok, *J. Neurophysiol.*, 2016, **115**, 1389–1398.
9 M. Riedel, M. J. Schwarz, M. Strassnig, I. Spellmann, A. Müller-Arends, K. Weber, J. Zach, N. Müller and H. J. Möller, *Eur. Arch. Psychiatry Clin. Neurosci.*, 2005, **255**, 261–268.
10 A. Rossi, F. Cañas, A. Fagiolini, I. Larmo, P. Levy, J. M. Montes, G. Papageorgiou, R. Sturlason, M. Zink and C. U. Correll, *Postgrad. Med.*, 2011, **123**, 135–159.
11 A. Salmoiraghi and M. Odiyoor, *J. Psychopharmacol.*, 2006, **20**, 592–593.
12 A. A. Shirzadi and S. N. Ghaemi, *Harv. Rev. Psychiatry*, 2006, **14**, 152–164.
13 E. A. Nunes, E. M. Mackenzie, D. Rossolatos, J. Perez-Parada, G. B. Baker and S. M. Dursun, *Expert Rev. Neurother.*, 2012, **12**, 801–812.
14 K. Wichapong, A. Nueangaudom, S. Pianwanit, F. Tanaka and S. Kokpol, *Mol. Simul.*, 2014, **40**, 1167–1189.
15 R. E. Williams and E. A. Lock, *Toxicology*, 2005, **207**, 35–48.
16 K. Hashimoto, Y. Fujita, M. Horio, S. Kunitachi, M. Iyo, D. Ferraris and T. Tsukamoto, *Biol. Psychiatry*, 2009, **65**, 1103–1106.
17 H. Mao, Y. Fujita, T. Ishima, M. Iyo, D. Ferraris, T. Tsukamoto and K. Hashimoto, *Open Clin. Chem. J.*, 2009, **2**, 16–21.
18 T. Adage, A. C. Trillat, A. Quattropani, D. Perrin, L. Cavarec, J. Shaw, O. Guerassimenko, C. Giachetti, B. Gréco, I. Chumakov, S. Halazy, A. Roach and P. Zaratin, *Eur. Neuropsychopharmacol.*, 2008, **18**, 200–214.

19 S. M. Smith, J. M. Uslaner, L. Yao, C. M. Mullins, N. O. Surles, S. L. Huszar, C. H. McNaughton, D. M. Pascarella, M. Kandebo, R. M. Hinchliffe, T. Sparey, N. J. Brandon, B. Jones, S. Venkatraman, M. B. Young, N. Sachs, M. A. Jacobson and P. H. Hutson, *J. Pharmacol. Exp. Ther.*, 2009, **328**, 921–930.

20 N. Hin, B. Duvall, J. F. Berry, D. V. Ferraris, R. Rais, J. Alt, C. Rojas, B. S. Slusher and T. Tsukamoto, *Bioorg. Med. Chem. Lett.*, 2016, **26**, 2088–2091.

21 A. J. Duplantier, S. L. Becker, M. J. Bohanon, K. A. Borzilleri, B. A. Chrunyk, J. T. Downs, L. Y. Hu, A. El-Kattan, L. C. James, S. Liu, J. Lu, N. Maklad, M. N. Mansour, S. Mente, M. A. Piotrowski, S. M. Sakya, S. Sheehan, S. J. Steyn, C. A. Strick, V. A. Williams and L. Zhang, *J. Med. Chem.*, 2009, **52**, 3576–3585.

22 S. C. Zimmermann, R. Rais, J. Alt, C. Burzynski, B. S. Slusher and T. Tsukamoto, *ACS Med. Chem. Lett.*, 2014, **5**, 1251–1253.

23 J. F. Berry, D. V. Ferraris, B. Duvall, N. Hin, R. Rais, J. Alt, A. G. Thomas, C. Rojas, K. Hashimoto, B. S. Slusher and T. Tsukamoto, *ACS Med. Chem. Lett.*, 2012, **3**, 839–843.

24 T. Hondo, M. Warizaya, T. Niimi, I. Namatame, T. Yamaguchi, K. Nakanishi, T. Hamajima, K. Harada, H. Sakashita, Y. Matsumoto, M. Orita and M. Takeuchi, *J. Med. Chem.*, 2013, **56**, 3582–3592.

25 N. Hin, B. Duvall, D. Ferraris, J. Alt, A. G. Thomas, R. Rais, C. Rojas, Y. Wu, K. M. Wozniak, B. S. Slusher and T. Tsukamoto, *J. Med. Chem.*, 2015, **58**, 7258–7272.

26 S. P. Mandal, M. A. Garg, S. S. Sahetya, S. R. Nagendra, H. S. Sripad, M. M. Manjunath, S. M. Soni, R. N. Baig, S. V. Kumar and B. R. Prashantha Kumar, *RSC Adv.*, 2016, **6**, 58641–58653.

27 Z. Qin, M. Wang and A. Yan, *Bioorg. Med. Chem. Lett.*, 2017, **27**, 2931–2938.

28 E. Cichero, C. Brullo, O. Bruno and P. Fossa, *RSC Adv.*, 2016, **6**, 61088–61108.

29 S. Patel, B. Patel and H. Bhatt, *J. Taiwan Inst. Chem. Eng.*, 2016, **59**, 61–68.

30 J. Gasteiger and M. Marsili, *Tetrahedron*, 1980, **36**, 3219–3228.

31 M. Clark, R. D. Cramer and N. V. Oppenbosch, *J. Comput. Chem.*, 1989, **10**, 982–1012.

32 R. D. Cramer, D. E. Patterson and J. D. Bunce, *J. Am. Chem. Soc.*, 1988, **110**, 5959–5967.

33 G. Klebe, U. Abraham and T. Mietzner, *J. Med. Chem.*, 1994, **37**, 4130–4146.

34 S. V. Jain, M. Ghate, K. S. Bhadoriya, S. B. Bari, A. Chaudhari and J. S. Borse, *Org. Med. Chem. Lett.*, 2012, **2**, 1–13.

35 M. Böhm, J. Stürzebecher and G. Klebe, *J. Med. Chem.*, 1999, **42**, 458–477.

36 U. Norinder, *Perspect. Drug Discovery Des.*, 1998, **12**, 25–39.

37 E. Alciaturi, C. E. Scobar, E. Marcos, D. L. Cruz and C. Rincón, *Rev. Tec. Fac. Ing., Univ. Zulia*, 2003, **26**, 197–204.

38 P. P. Roy, J. T. Leonard and K. Roy, *Chemom. Intell. Lab. Syst.*, 2008, **90**, 31–42.

39 T. Chai and R. R. Draxler, *Geosci. Model Dev.*, 2014, **7**, 1247–1250.

40 K. Roy, P. Ambure and R. B. Aher, *Chemom. Intell. Lab. Syst.*, 2017, **162**, 44–54.

41 A. R. Leach, B. K. Shoichet and C. E. Peishoff, *J. Med. Chem.*, 2006, **49**, 5851–5855.

42 A. Daina, O. Michielin and V. Zoete, *Sci. Rep.*, 2017, **7**, 42717.

43 M. Remko, *Comput. Theor. Chem.*, 2009, **897**, 73–82.

44 R. B. Silverman, *The Organic Chemistry of Drug Design and Drug Action*, Elsevier, Amsterdam, 2nd edn, 2004.

45 T. Tsukamoto, B. S. Slusher, D. V. Ferraris, C. Rojas, N. Hin B. Duvall, *US Pat.* 9505753B2, 2016.

46 W. Shen and Y. H. Lu, *Bangladesh J. Pharmacol.*, 2013, **8**, 156–170.